PURPOSE-LED PUBLISHING™

LETTER • **OPEN ACCESS**

Graphene Josephson diodes from asymmetric disorder

To cite this article: Ivan Villani *et al* 2026 *2D Mater.* **13** 041001

View the article online for updates and enhancements.

You may also like

- Hydrogen transport within graphene multilayers by means of flexural phonons
Vito Dario Camiola, Riccardo Farchioni, Vittorio Pellegrini et al.
- Thermal stability of monolayer WS_2 in BEOL conditions
Simona Pace, Marzia Ferrera, Domenica Convertino et al.
- Leaf water diffusion dynamics in vivo through a sub-terahertz portable imaging system
F V Di Girolamo, A Toncelli, A Tredicucci et al.

This content was downloaded from IP address 192.167.204.120 on 29/10/2026 at 08:06

2D Materials

Check for updates

OPEN ACCESS

RECEIVED
15 June 2026

REVISED
28 August 2026

ACCEPTED FOR PUBLICATION
19 October 2026

PUBLISHED
29 October 2026

Original content from this work may be used under the terms of the Creative Commons Attribution 4.0 licence.

Any further distribution of this work must maintain attribution to the author(s) and the title of the work, journal citation and DOI.

LETTER

Graphene Josephson diodes from asymmetric disorder

Ivan Villani[1], Luca Chirolli[2], Matteo Carrega[3], Alessandro Crippa[1], Elia Strambini[1], Francesco Giazotto[1], Vaidotas Mišeikis[4], Camilla Coletti[4], Fabio Beltram[1], Kenji Watanabe[5], Takashi Taniguchi[6], Stefan Heun[1,*] and Sergio Pezzini[1,*]

[1] Istituto Nanoscienze–CNR, NEST-Scuola Normale Superiore, Piazza San Silvestro 12, 56127 Pisa, Italy
[2] Department of Physics and Astronomy, University of Florence, 50019 Sesto Fiorentino, Italy
[3] CNR-SPIN, Via Dodecaneso 33, 16146 Genova, Italy
[4] Center for Nanotechnology Innovation, Laboratorio NEST, Istituto Italiano di Tecnologia, 56127 Pisa, Italy
[5] Research Center for Electronic and Optical Materials, National Institute for Materials Science, 1-1 Namiki, Tsukuba 305-0044, Japan
[6] Research Center for Materials Nanoarchitectonics, National Institute for Materials Science, 1-1 Namiki, Tsukuba 305-0044, Japan
[*] Authors to whom any correspondence should be addressed.

E-mail: stefan.heun@cnr.it and sergio.pezzini@cnr.it

Keywords: graphene, Josephson junction, supercurrent diode

Supplementary material for this article is available online

Abstract

Josephson diodes are non-reciprocal superconducting devices characterized by different switching currents depending on the current flow direction. They recently attracted considerable theoretical and experimental attention, in view of their possible application as rectifying elements in the field of superconducting electronics, and as probes to investigate symmetry breaking mechanisms in mesoscopic systems. In this work, we show that graphene Josephson junctions provide rectification of supercurrent with an efficiency exceeding 20%. The effect appears applying a mT out-of-plane magnetic field and is enhanced close to the nodes of the Fraunhofer interference pattern. Our findings are consistent with a theoretical model that considers long-range scattering potentials in the junction as the symmetry-breaking mechanism, which yields supercurrent rectification in highly transparent junctions. While graphene stands out as an ultra-clean transmission medium, our work shows that unavoidable residual disorder is sufficient to promote this effect.

1. Introduction

In modern electronics, the standard diode represents a fundamental non-reciprocal device that provides current rectification. The diode finds widespread applications in AC to DC current conversion, circuit protection (Zener diodes), high-speed applications (Schottky diodes), or as light emitting and photodiodes [1]. The most common diode implementation is based on a p–n semiconductor junction that explicitly breaks the spatial inversion symmetry.

A supercurrent diode represents the superconducting counterpart of the standard diode: it provides rectification of a supercurrent, that is, for a given range of parameters, it exhibits zero-resistance only for one direction of current flow. The simultaneous breaking of inversion and time-reversal symmetries has been identified as necessary condition for a system to exhibit supercurrent rectification [2–4], as this breaks the equivalence between the positive and negative propagation directions.

The supercurrent diode received limited attention until 2020, when Ando and coworkers [5] observed the effect in a $[Nb/V/Ta]_n$ superlattice lacking inversion symmetry. In this case, the origin of the superconducting diode effect lies in the magnetochiral anisotropy induced by the simultaneous breaking of spatial inversion symmetry and time-reversal symmetry. The latter was broken by applying an external in-plane magnetic field perpendicular to the current flow. This anisotropy results in a nonreciprocal critical current, which enables zero-resistance for one direction of current flow.

This first experimental report immediately promoted a tremendous interest in the field, and extensive efforts both on the theoretical [4, 6–18] and experimental side [19–53] have been made to investigate and improve a variety of platforms in terms of efficiency and tunability. Furthermore, the diode serves as a powerful tool to identify non-trivial symmetry breaking mechanisms. Several supercurrent diode realizations rely on

© 2026 The Author(s). Published by IOP Publishing Ltd

the application of a magnetic field, both in-plane [19–22, 24–26, 54] and out-of-plane [27–35]. The effect can also be sustained by synthetic magnetic fields, or obtained in samples with optimized geometric layouts, thus not relying on the application of external fields [36–40, 42–44, 49].

Some of these implementations are based on Josephson junctions, which provide a wide flexibility in terms of geometry, materials choice, and additional tuning knobs such as electrostatic gating and supercurrent modulation. In those cases the diodicity pertains the switching current of the junction, and the phenomenon is known as Josephson diode effect (JDE) – which differs from the superconducting diode effect (SDE) that affects the critical current of a bulk superconductor as a whole. In Josephson junctions based on materials with large spin–orbit interaction, such as InSb [22], InAs [24, 26], or InGaAs [25], the JDE emerges from the simultaneous breaking of inversion and time-reversal symmetries through the interplay of Rashba spin–orbit interaction and an external in-plane magnetic field. This combination induces an asymmetric current-phase relation characterized by an anomalous phase shift and cosine harmonics, which ultimately leads to a direction-dependent critical current [55]. For the Rashba spin–orbit coupling that breaks mirror symmetry about the direction perpendicular to the junction plane, the JDE takes place under the application of an in-plane magnetic field directed perpendicular to the current [6]. The JDE was also reported for gate-defined graphene junctions, when multiple layers are twisted at the so-called magic-angle [30, 56]. This phenomenology is based on correlation-driven phases with valley polarization and orbital magnetism [57], that are however obtained at the cost of complex fabrication routes [58]. Recent results indicate that the JDE in this class of systems can also be driven by disorder, specifically due to twist angle variations along the device [53].

In this work, we focus on Josephson junctions built from a single layer of graphene encapsulated in hexagonal boron nitride (hBN) [59], a platform with negligible spin–orbit coupling [60], no correlated electronic phases, and among the cleanest two-dimensional electron systems [61]. We find that these devices exhibit a JDE with rectification efficiency of more than 20% under a purely out-of-plane magnetic field. The two conditions of breaking the time reversal and inversion symmetries, which are necessary (but not sufficient) for the JDE to appear, are satisfied as follows. The time reversal symmetry is explicitly broken by the magnetic field. This also implies that the diode effect is ruled out at $B = 0$, which is in agreement with our experimental observations. Regarding inversion symmetry breaking, we consider residual long-range disorder that is present even in graphene/hBN stacks [61, 62]. Guided by a theoretical model originally developed for a two-dimensional electron gas (2DEG) [63] and tailored to the case of graphene, we identify a specific mirror symmetry breaking in the scattering potential as necessary condition for the JDE. The relevant vector $\mathbf{M_x}$ defining this symmetry plane is perpendicular to magnetic field $\mathbf{B}$ (directed along z) and the current direction $\mathbf{I}$ (so it is parallel to their cross-product: $\mathbf{M_x} \parallel \mathbf{I} \times \mathbf{B}$), as indicated in figure 1(a). In a two-dimensional system, this translates to a mirror symmetry breaking about the dashed blue axis in the figure.

In our experiment, the JDE emerges in the Fraunhofer interference patterns, i.e. in presence of an out-of-plane magnetic field. Fraunhofer patterns differ depending on the direction of the current flow. Supercurrent rectification is observed within the main Fraunhofer lobe and enhanced at the first nodes. Beyond the first nodes, the diode behavior becomes more unpredictable, as it is strongly influenced by the details of the potential landscape.

2. Experimental results

2.1. Investigated devices

We study the JDE in hBN-encapsulated graphene Josephson junctions contacted by Niobium (Nb) leads and supported by a Si/SiO_2 substrate acting as back-gate (a device schematics is shown in figure 1(a)). Two Josephson junctions D1 and D2 were studied in this work, fabricated according to the same fabrication protocol (reported in [64], more details are presented in the Methods), but belonging to different samples fabricated independently at a time interval of several months. Both devices have length $L = 400$ nm and width $W = 3\ \mu$m, and are based on high-quality graphene single crystals grown by chemical vapor deposition (CVD) [65–67]. Measurements on device D1 were performed in a Leiden Cryogenics dilution refrigerator, at a base temperature of 40 mK, while measurements on device D2 were performed in a continuous flow ICE ^{3}He refrigerator, at a base temperature of 350 mK. Both cryostats are equipped with electronic filters anchored to the lowest-temperature plate, comprising double stage RC filters and a π-filter stage. We report data from device D1 in the main text, while data from device D2 are reported in the Supplementary material.

The devices show electrical transport characteristics in line with hBN-encapsulated graphene Josephson junctions reported in the literature [59, 68]. The induced superconductivity is strongly modulated by the voltage applied to the back-gate (V_{BG}), as illustrated in the Supplementary material, section S1.1. The supercurrent reaches more than 10 μA thanks to the large interface transparency (Tr up to 0.73 and 0.84, for devices D1 and D2, respectively, calculated from the normal state resistance following the procedure outlined in [68];

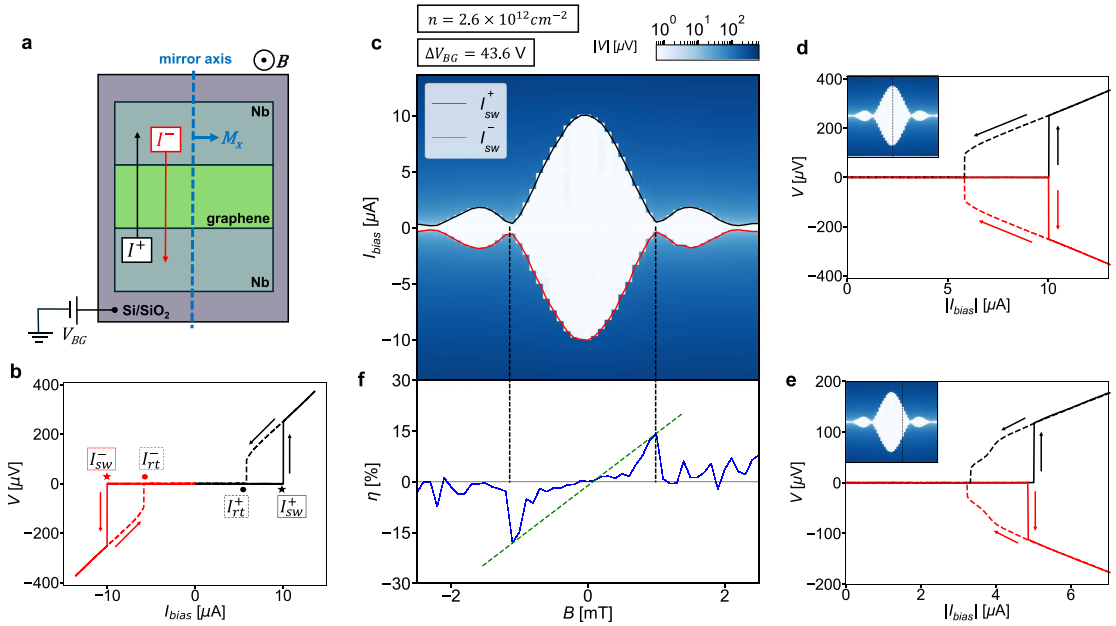


Figure 1. (a) Top view schematics of device layout. Graphene is encapsulated in hBN and edge-contacted by Nb leads. The heterostructure is placed on top of a Si/SiO_2 substrate, which acts as a back-gate via the application of a back-gate voltage V_{BG}. A current I is applied and flows through the junction, and the voltage drop is measured. Currents flowing in either positive (I^+) or negative (I^-) directions are indicated in black and red respectively. Magnetic field B is applied in the out-of-plane direction. Mirror symmetry axis M_x is indicated. (b) Voltage–current (V–I) curve at $B = 0$ showing switching-retrapping behavior. Positive and negative flowing currents are represented in black and red, respectively, with the same notation as in a. The sweep direction of the current is indicated by the arrows. Solid lines indicate the switching branches, while dashed lines indicate the retrapping branches. Positive (I_{sw}^+) and negative (I_{sw}^-) switching currents are indicated respectively by the black and red stars, while positive (I_{rt}^+) and negative (I_{rt}^-) retrapping currents by black and red dots. (c) Fraunhofer pattern (voltage drop $|V|$ as function of magnetic field B and DC current bias $I_{\rm bias}$): $V_{\rm BG} = 40$ V ($\Delta V_{\rm BG} = 43.6$ V, $n = 2.6 \times 10^{12}$ cm^{-2}). (d–e) V–I curves taken at $B = 0$ mT and $B = 0.6$ mT respectively, corresponding to the black dashed lines in the insets, plotted as function of $|I_{\rm bias}|$. Black and red lines indicate respectively positive and negative flowing currents, following the same notation as in a and b, while arrows indicate the sweep direction. In d, no diode effect is observed, i.e. positive and negative switching (and retrapping) currents coincide, while they are different in e. (f) Diode rectification coefficient η as a function of magnetic field B, calculated using equation (1). We define the polarity of the diode as the sign of the slope of the green dashed line, traced by connecting peaks in η at first nodes. In this case, the diode has positive polarity. $T = 40$ mK for b–f.

see also Supplementary material), with comparable values measured for the two devices. Additional characterization of device D1 is provided in the Supplementary material, section S1.1. The junctions show a pronounced switching-retrapping behavior, as shown in figure 1(b), where we report a representative $V - I$ curve at zero magnetic field, with the corresponding sweep directions indicated by arrows. I_{sw}^+ and I_{sw}^- indicate the switching currents in the positive and negative flow direction, I_{rt}^+ and I_{rt}^- the corresponding retrapping currents (the lower value of the retrapping current originates from a self-heating effect [69]). In this work, we use the term *critical current* to identify simulation results, while we use the term *switching current* to identify the experimental results. The measured switching current is used as an experimental estimate of the *critical current* of the Josephson junction.

2.2. JDE observation

A Fraunhofer interference pattern is observed upon application of an out-of-plane magnetic field, as expected for extended junctions, resulting from the interference of the supercurrent as magnetic flux threads the junction area. In our devices, Fraunhofer patterns are different depending on the direction of current flow. This is a manifestation of the JDE. The effect is observed within the main and first lateral lobes. Therefore, all Fraunhofer acquisitions reported here were limited to a ± 2.5 mT range (Fraunhofer patterns of device D1 in an extended ± 10 mT range are shown in the Supplementary material, section S1.1). In figure 1(c) we show the Fraunhofer interference pattern at large electron doping, $\Delta V_{\rm BG} = 43.6$ V. $\Delta V_{\rm BG}$ is defined relative to the charge neutrality point (CNP), $\Delta V_{\rm BG} = V_{\rm BG} - V_{\rm BG}^{\rm CNP}$ ($V_{\rm BG} = 40$ V in figure 1(c)). For device D1, $V_{\rm BG}^{\rm CNP} = -3.6$ V, a typical value for Nb-contacted graphene [68]. The data in the color map is obtained by sweeping the current bias from zero, highlighting the positive and negative switching currents (black and red lines, respectively). The JDE is illustrated in detail in figures 1(d) and (e), where we report the positive and negative switching and retrapping sweeps from the pattern shown in figure 1(c), at two different magnetic field values. In figure 1(d), taken at $B = 0$ (black dashed line in the inset of figure 1(d)), $I_{sw}^+ = |I_{sw}^-|$ and $I_{rt}^+ = |I_{rt}^-|$, i.e. no JDE is observed. Conversely, in figure 1(e),

taken at $B = 0.6$ mT (black dashed line in the inset of figure 1(e)), $I_{sw}^{+} \neq |I_{sw}^{-}|$ and $I_{rt}^{+} \neq |I_{rt}^{-}|$, hence we observe supercurrent rectification. We remark that the JDE is observed in both switching (I_{sw}, continuous lines in figure 1(b)) and retrapping directions (I_{rt}, dashed lines in figure 1(b)). The lower value of the retrapping current is caused by a self-heating effect (thus, the mechanism for supercurrent rectification is the same for switching and retrapping currents). In the following discussion on JDE, we focus on the switching current. Comparable results are obtained for the retrapping current and are shown in the Supplementary material, section S1.2.

The efficiency of a supercurrent diode is given by the rectification parameter η, defined as the ratio between the difference and the sum of the switching currents propagating in opposite directions:

$$\eta = \frac{I_{sw}^{+} - |I_{sw}^{-}|}{I_{sw}^{+} + |I_{sw}^{-}|}. \tag{1}$$

The diode efficiency η for the data shown in figure 1(c) is reported in figure 1(f) as a function of magnetic field B. The rectification parameter shows a characteristic anti-symmetric shape, indicating that time-reversal symmetry is broken only for $B \neq 0$, and that a reversal of the magnetic field maps I_{sw}^{+} onto I_{sw}^{-} and vice-versa. η is enhanced at the field values corresponding to the first Fraunhofer nodes, and is, in this case, negligible within the first lateral lobes. We note that even at the nodes I_{sw}^{+} and I_{sw}^{-} remain of the order of several hundreds of nA. In this context, a relevant complementary metric to assess the diode performance is provided by the absolute switching current difference $\Delta I_{sw} = I_{sw}^{+} - |I_{sw}^{-}|$. For the case presented in figure 1(c), at the Fraunhofer node at $B = -1.1$ mT, $I_{sw}^{+} = 385$ nA, $I_{sw}^{-} = -555$ nA, resulting in $\Delta I_{sw} = -170$ nA. The maximum $\Delta I_{sw} = -453$ nA, instead, is observed at slightly lower magnetic field ($B = -0.8$ mT), where the switching currents already exceed 3 μA. Additional data and discussion are provided in section S1.3 of the Supplementary material. We define the polarity of the diode as the sign of the slope of the line obtained by connecting the peaks in η at the first nodes. For the case presented in figure 1(f), the sign of the slope of the green dashed line is positive, so the diode has positive polarity.

In figures 2(b), (d) and (f) we report Fraunhofer patterns at different back-gate voltages, respectively at $V_{BG} = -20, 0, +20$ V, at the positions indicated in the back-gate sweep of the normal-state resistance R shown in figure 2(a). Due to the aforementioned $V_{BG}^{CNP} = -3.6$ V, the junction is hole-doped at $V_{BG} = -20$ V, while for $V_{BG} = 0, +20$ V, the junction is electron-doped. This set of measurements thus allows to evaluate the JDE as the carrier density is varied. The carrier density is $n = C_g(V_{BG} - V_{BG}^{CNP})$, where $C_g = 6 \times 10^{10}\text{cm}^{-2}\text{V}^{-1}$ is the back-gate lever arm for our gating configuration [67], which is also reported as the top x-axis in figure 2(a) and for each Fraunhofer pattern. In figures 2(c), (e) and (g) we report the corresponding rectification coefficients (blue lines), along with positive and negative switching currents (black and red lines) normalized to the maximum value (since the supercurrent is modulated by V_{BG}, the maximum supercurrent is different for the three patterns). All three patterns exhibit supercurrent rectification within the main Fraunhofer lobe, with enhanced η at the nodes, and they share the same diode polarity. However, differences are present, with larger maxima in the diode efficiency at the first node visible in figures 2(b) and (c), where η exceeds 20%. In figures 2(d) and (e), at $V_{BG} = 0$ V, we obtain the JDE notably in gate-free operation. In this case, η is clearly non-zero also on the first lateral lobes, while negligible rectification is observed on the first lateral lobes in figures 2(f) and (g) (similar to figures 1(c) and (f)). As we will show in the following, this variability is captured by our theoretical model and determined by the interplay of microscopic details in the disorder and the chemical potential set by V_{BG}. Similar results are obtained for device D2 and for an additional device D3 with different geometry, presented in the Supplementary material, sections S2 and S3.

3. Theoretical model

The theoretical description of the JDE in the Fraunhofer patterns of planar Josephson junctions has been provided in [63] for the case of a 2DEG. It was shown that the diode effect is originated by the breaking of the mirror symmetry of the junction about the $\mathbf{M_x}$ axis due to an asymmetry in the scattering potential in the central region of the junction. This is sufficient to yield the diode effect in highly transparent Josephson junctions, in combination with an out-of-plane magnetic field which breaks the time-reversal symmetry. All relevant details about the scattering matrix model are summarized in the Supplementary material, section S4.

For the present case, the theoretical model has been adapted to the case of graphene. We model the graphene sheet by a tight-binding Hamiltonian:

$$H = -t \sum_{<ij>s} \left(e^{i\gamma_{ij}} c_{is}^{\dagger} c_{js} + H.c. \right) + \sum_{js} \left(V_j - \mu \right) c_{js}^{\dagger} c_{js}, \tag{2}$$

where c_{js} is a fermionic annihilation operator describing an electron with spin s at site j, which hops in a honeycomb lattice and picks up a phase $\gamma_{ij} = \frac{e}{\hbar} \int_{\mathbf{r_i}}^{\mathbf{r_j}} \mathbf{ds} \cdot \mathbf{A}(\mathbf{s})$ due to a uniform magnetic field $\mathbf{B}$ described by the vector potential $\mathbf{A} = \frac{1}{2}\mathbf{r} \times \mathbf{B}$ in the symmetric gauge. μ is the chemical potential and $V_j \equiv V(x_j, y_j)$ is a potential experienced by electrons and describing the effect of long range disorder. The

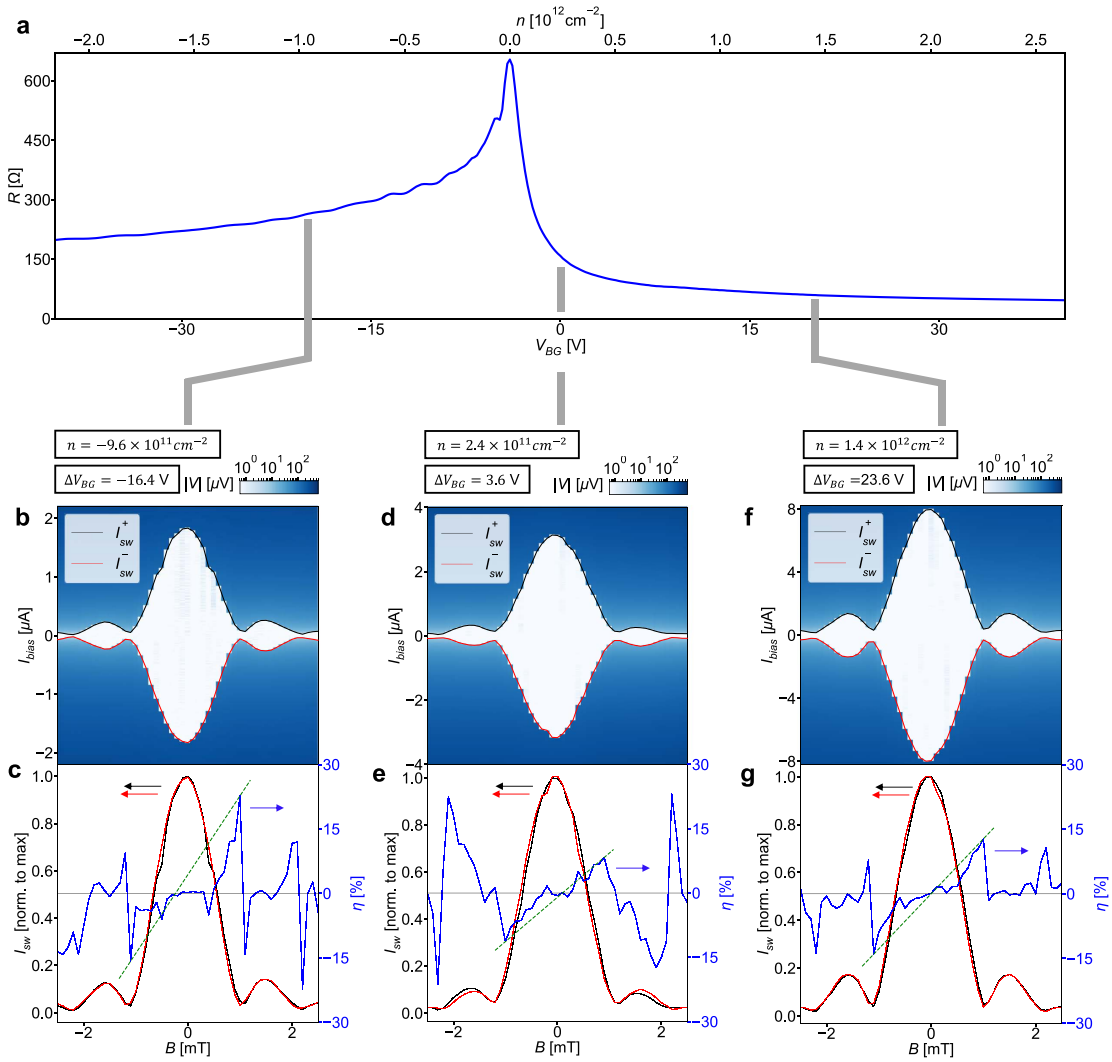


Figure 2. (a) Back-gate sweep: sample resistance R as a function of back-gate voltage V_{BG} (lower x-axis), measured by applying a large DC current bias. The top x-axis shows the corresponding charge carrier density n. The acquisition position of the Fraunhofer patterns in b,d,f is indicated. $T = 4.2$ K, $B = 0$ T. (b–g) *Upper row*: Fraunhofer patterns (voltage drop $|V|$ as function of out-of-plane magnetic field B and DC bias current I_{bias}). *Lower row*: corresponding rectification parameter η at different back-gate voltage values. The relative position to the charge neutrality point $\Delta V_{\mathrm{BG}} = V_{\mathrm{BG}} - V_{\mathrm{CNP}}$ ($V_{\mathrm{CNP}} = -3.6$ V) and the corresponding charge carrier density values are indicated at the top of each panel. (b-c) $V_{\mathrm{BG}} = -20$ V. (d-e) $V_{\mathrm{BG}} = 0$ V. (f-g) $V_{\mathrm{BG}} = +20$ V. $T = 40$ mK for b-g.

back-gate is assumed to globally change the chemical potential μ. In pristine graphene, $t = 2.7$ eV is the nearest neighbor hopping energy [60]. In the simulations, t is a reference energy scale. Given the size of the simulated system with an effective lattice spacing a, the low-energy dynamics around the Dirac point is recovered by setting the Dirac velocity to $v_{\mathrm{D}} = 3at/2$.

3.1. Highly doped junctions with different disorder

Far away from the Dirac point, a doped graphene sheet behaves very much like an ordinary 2DEG, with the only difference that the sites j are now on a honeycomb lattice and the Hamiltonian is that of equation (2). In figures 3(a) and (d) we report two different potentials, $V_1(\mathbf{r}) = Vf_1(\mathbf{r})$ and $V_2(\mathbf{r}) = Vf_2(\mathbf{r})$, shown for $V = V_{\max} = 0.01t = 27$ meV as a function of spatial coordinates, expressed in units of the effective lattice spacing. Here, $f_1(\mathbf{r})$ and $f_2(\mathbf{r})$ are two different non-$\mathbf{M_x}$ symmetric functions describing the spatial evolution of the potential landscape. They are chosen such that $\max_{\mathbf{r}} f_i = -\min_{\mathbf{r}} f_i = 1$, and the geometrical aspect ratio x/y is the same as for the measured devices ($W/L = 7.5$). $V_{\max}$ is set to match the energy scale of the typical charge-fluctuation density of encapsulated graphene devices. For device D1 we obtain a charge-fluctuation density $n^* = 3.4 \times 10^{10}$ cm^{-2} that corresponds to 22 meV according to the Dirac relation [60] (for D2 $n^* = 1.9 \times 10^{10}$ cm^{-2}, corresponding to 16 meV); $n^\star$ values are obtained using the method outlined in [67] and are in line with previous reports of high-quality graphene Josephson junctions [61, 68]. It is therefore reasonable to expect the disorder potential in our devices to be analogous to other state-of-the-art hBN-encapsulated graphene Josephson junctions

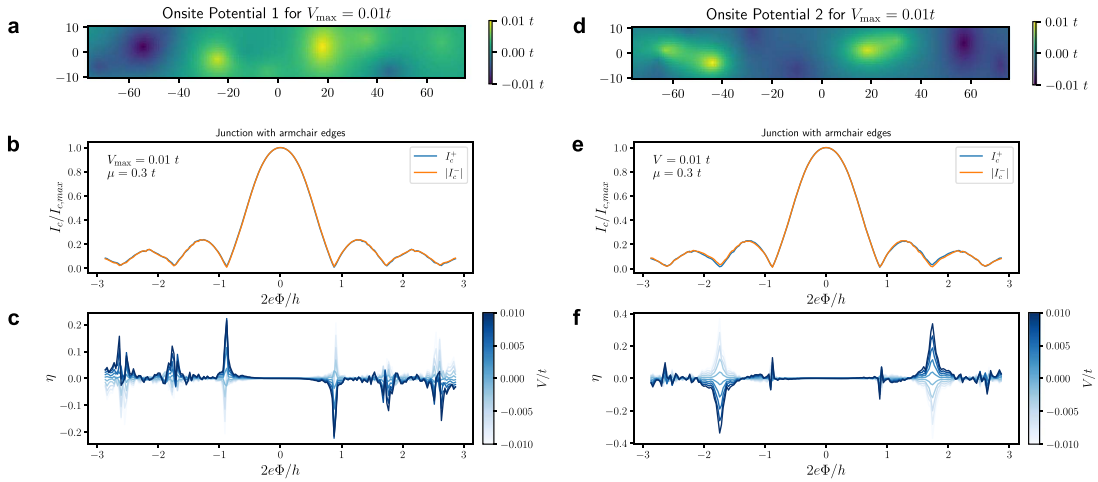


Figure 3. (a) Onsite potential $V_1(r) = Vf_1(r)$ for $V = V_{max} = 0.01\ t$. The spatial coordinates are in units of the effective lattice spacing. (b) Calculated Fraunhofer patterns (I_c^+ and $|I_c^-|$) for $V = V_{max}$ and chemical potential $\mu = 0.3t$. (c) Color-coded evolution of the rectification coefficient η for varying V in the range $-V_{max} < V < V_{max}$, as a function of applied magnetic flux $2e\Phi/h$. (d) Onsite potential $V_2(r) = Vf_2(r)$ for $V = V_{max} = 0.01\ t$. (e-f) Same as b and c, but for the onsite potential V_2 shown in d.

[59, 68, 69]. Further details are provided in the Supplementary material. The two simulated scattering potentials have a different long-range scattering center layout, but comparable characteristic spatial scales, with maxima and minima alternating on the scale of tens of effective lattice constants, corresponding to few hundreds of nm. In the resulting Fraunhofer patterns shown in figures 3(b) and (e), different I_c^+ and $|I_c^-|$ are visible.

In figures 3(c) and (f) we show the rectification coefficient η calculated for different values of the amplitude V of the potential landscape $-V_{max} < V < V_{max}$. Results in figure 3(c) are obtained for the potential V_1, while in figure 3(f) we show the rectification induced by the potential V_2. For the two potentials, the rectification parameter evolves in different ways with magnetic flux, showing that a device-specific pattern is to be expected related to the microscopic configuration of the scattering potential. Moreover, the effect always retains certain general features. For both potentials, a non-zero rectification coefficient η is obtained, which is enhanced in proximity to the nodes of the Fraunhofer pattern and antisymmetric around $B = 0$. Our experimental results show a rectification coefficient η that is either finite (figure 2(e)) or very low (figures 1(d), 2(c) and (g)) within the main Fraunhofer lobe, and antisymmetric around $B = 0$. In all cases, it is enhanced at the first Fraunhofer nodes, consistent with the theoretical simulations shown in figure 3.

Although we cannot directly tune the scattering potential in the experiment, we can compare the JDE in different devices with different microscopic realizations of the disorder. Since the normal-state characteristics $R(V_{BG})$ and the charge fluctuations n^* are comparable for devices D1 and D2 (see figure 2(a) and Supplementary material figures S1(e), S5(a) and (g)), the amplitude of the scattering potential is expected to be similar as well. A notable difference lies however in the shape of the Fraunhofer patterns of the two devices. While for D1 they appear to be more irregular (see Supplementary material, section S1.1), for D2 they are closer to the expected $\sin(x)/x$ form (see Supplementary material, section S2.1). It is therefore reasonable to assume that the two devices provide two different microscopic realizations of the disorder potential. Despite this difference, they exhibit a similar JDE—both in terms of magnitude of the rectification coefficient η and its dependence on the magnetic field—in accordance with our simulations considering scattering potentials with different shapes and amplitude.

3.2. Dependence on edge termination and chemical potential

In figure 4 we plot the simulated Fraunhofer patterns for the same potential V_1 as in figure 3(a), shown in figure 4(a), for two nominally identical graphene sheets, only differing by their relative orientation, with armchair edges in (b) and (c), as schematized in (d), and with zigzag edges in (e) and (f), as schematized in (g). In figures 4(b) and (e) the chemical potential is set to $\mu = 0.3\ t$ and Fraunhofer patterns with different I_c^+ and $|I_c^-|$ are obtained. In figures 4(c) and (f) we study the variation of the rectification coefficient η with chemical potential μ varying across the Dirac point, located at $\mu = 0$. Comparing figures 4(c) and (f), we note that no relevant differences are observed that would depend on the relative orientation of the graphene edges. We remark that, by using common plasma etching techniques, this parameter cannot be experimentally controlled, resulting in edges comprising a random combination of the two terminations.

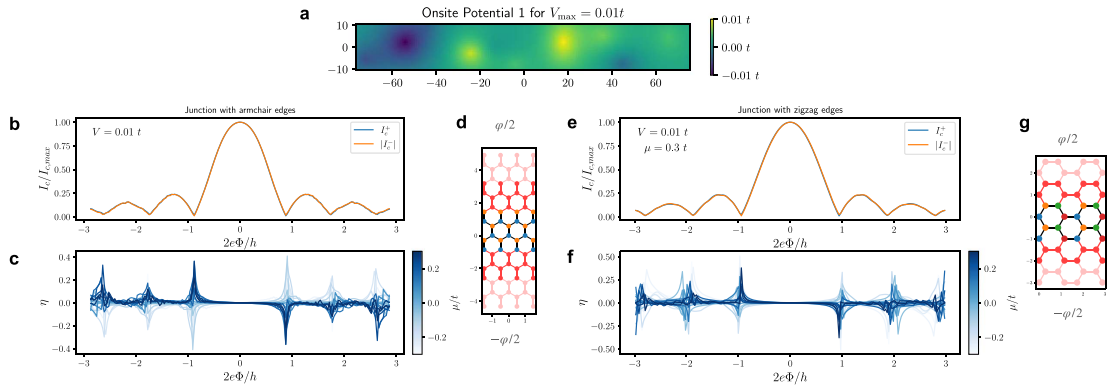


Figure 4. (a) Onsite potential V_1 for $V = V_{max} = 0.01\ t$. (b) Calculated Fraunhofer patterns (I_c^+ and $|I_c^-|$) for the case of armchair edges for $\mu = 0.3t$. (c) Color-coded evolution of the rectification coefficient η with chemical potential μ, crossing the Dirac point. (d) Graphene strip with armachair edges. (e-f) Same as b and c, but for a graphene strip with zigzag edges as shown in g.

The rectification coefficient in figures 4(c) and (f) shows enhanced values around all nodes of the Fraunhofer pattern and variations with the chemical potential. We experimentally observe similar variations in our devices as V_{BG} is changed. For example, η is clearly non-zero in the first lateral lobes in figure 2(d), while its value is very small in other cases. It is important to note that the character of the variation with μ does not always show effective tunability with the sign of the chemical potential. This is reasonable, in that a change of sign of the chemical potential maps electron-like excitations to hole-like excitations, which experience a potential $-V$ of opposite sign. The latter is in general different from its mirror symmetric form $M_x^{-1}VM_x$ (M_x is the operator performing a mirror symmetry operation about the $\mathbf{M_x}$ plane in figure 1(a)), and a change of sign of the rectification coefficient is therefore not expected. Indeed, although in figure 4(c) we see a change of sign of the rectification with μ, this is not evident in figure 4(f). This is in agreement with our experimental observations, where no change in the diode polarity is observed in device D1 while crossing the CNP (see figures 2(c) and (e)), while it is observed in device D2, as shown in the Supplementary material, section 2.2. The polarity of these graphene Josephson diodes is determined by the details of the scattering potential, which cannot be directly controlled by acting on the back-gate. As discussed in the Supplementary material, section S5, a deterministic diode polarity flip is obtained by performing a mirror symmetry operation on the scattering potential about the $\mathbf{M_x}$-axis, but this control is experimentally challenging.

We next consider the case of chemical potential μ close to the Dirac point. This regime is dominated by strong density inhomogeneities, known as charge puddles [70]. Their formation drastically modifies the transport properties as compared to highly doped graphene [71]. A Fraunhofer pattern measured close to the CNP is shown in Supplementary material figure S4. We observe a distortion of the nterference pattern, with a partial merging of the main and first side lobes (i.e. a suppression of the first minima). Such shape can be qualitatively connected to changes in the supercurrent distribution, which could be reasonably expected in the charge puddle regime. However, when considering the JDE, there is no reason to expect substantial differences in the rectification coefficient as compared to the highly doped case. The diode is caused by an asymmetry in the electrostatic potential, which is present even in low doping regimes. Both in the experimental data and in the simulations, at low doping η exhibits comparable behavior to the large doping case in terms of amplitude and magnetic field dependence.

4. Discussion

To observe supercurrent rectification, it is necessary to simultaneously break the inversion and time-reversal symmetries. A common way to achieve this is by exploiting Rashba spin–orbit interation in combination with an in-plane magnetic field. Here we can rule out this mechanism because monolayer graphene presents negligible spin–orbit coupling [72]. We also do not expect any relevant contribution arising from interaction with the hexagonal Boron Nitride substrate [73, 74]. We can also exclude effects such as valley polarization and orbital magnetism found in moiré multilayers [30, 56, 57]. Moreover, we obtain supercurrent rectification without any specific geometrical engineering (such as the trapezoidal devices analyzed in [63] or the Josephson triodes presented in [36, 41]) that would lead to a geometrically induced supercurrent rectification. Finally, we recall that previous reports [33, 35] of JDE in out-of-plane magnetic fields identify the self-field generated by the supercurrent as the symmetry breaking mechanism. In this case, the JDE is predicted to be enhanced as the switching current increases, but

this is not consistent with our experimental observations. In fact, we observe maximum rectification at the minima of the Fraunhofer patterns. Here the self-field induced by the supercurrent is minimum and thus much smaller than close to the Fraunhofer maximum, where instead suppressed supercurrent rectification is observed. This is in contrast with the prediction of a larger rectification due to a larger self-field, and we therefore discard this explanation.

5. Conclusions

We have demonstrated that hBN-encapsulated graphene Josephson junctions exhibit supercurrent rectification upon the application of an out-of-plane magnetic field. Supercurrent rectification is observed in the Fraunhofer patterns, irrespective of doping level and carrier sign. All our experimental observations are consistent with an asymmetric scattering potential as the source for breaking of the mirror symmetry, enabling the JDE. Simulations of the rectification coefficient η under different conditions match well the experimental observations. In our simulations, we explored different potential shapes that break the required symmetries, all qualitatively similar but quantitatively different. Supercurrent rectification is observed in the main Fraunhofer lobe and enhanced at the first nodes. However, the details of the rectification coefficient depend on the shape of the potential, on its amplitude, and on the chemical potential. Such variability does not follow a specific trend, but it rather evolves in an uncontrolled way, which is consistent with the experimental data. Indeed, different devices set to different back-gate voltages realize a variety of configurations in terms of potential shape, amplitude and chemical potential: for this reason, quantitative agreement between experimental data and the simulations is not to be expected. However, the general behavior of η is consistently preserved: η is always antisymmetric around $B = 0$ and enhanced at the nodes, where it reaches values of approximately 20%. Beyond the first nodes, the character of the rectification coefficient depends crucially on the details of the scattering potential, as expected from the theoretical simulations. The diode polarity does not appear to be determined by the sign of the charge carriers, consistent with a non-polar nature of the scattering potential but is only affected by the details of the disorder, and for this reason, in our devices it is not directly controllable.

Our devices provide an easy-to-access proof-of-concept platform for supercurrent rectification, only requiring an out-of-plane magnetic field as external knob to exhibit the effect, and potentially serving as a probe to study symmetry breaking mechanisms in this mesoscopic system. Further engineering may provide the necessary elements for additional tunability for applications in the realm of superconducting electronics. For example, direct control of the scattering potential could be implemented by the use of additional side gates. These have been demonstrated on InSb nanoflag Josephson junctions [75, 76] and on graphene-based Josephson junctions [77] to be highly effective in tuning transport properties, not only in the normal regime, but also in the dissipation-less regime. They could be used to deterministically change the shape and symmetry of the scattering potential, thus possibly serving as tuning knobs for the JDE and its polarity. In conclusion, graphene Josephson junctions in mT magnetic fields represent a valid JDE platform, and we expect they could be further engineered to achieve broader and more reliable tunability of the JDE.

6. Methods

Fabrication of graphene Josephson junction devices starts from the assembly of the hBN-graphene-hBN stack, performed by employing the standard dry pick-up technique described in [67, 78, 79]. A poly(bisphenol A carbonate) (PC) film is deposited onto a polydimethylsiloxane (PDMS) [79] stamp, which is attached to a glass slide. This stamp is used to combine micromechanically exfoliated hBN flakes ($\sim$30 nm thick) and CVD-grown monolayer graphene single-crystals [65, 66], as described in [67]. After the assembly, Raman spectroscopy is used to identify target areas characterized by minimal nanoscale strain variations [67, 80, 81], in which devices are then located. Device patterning is done through electron beam lithography (EBL) employing a polymethylmethacrylate (PMMA) mask (AR-P 672.045 resist). The first EBL step defines a mask which is used for both etching and sputtering, leading to self-aligned one-dimensional superconducting contacts [68]. First, a 15 s mild oxygen plasma step (10 W power) is performed prior to etching to remove polymer residues in the exposed areas. A mixture of CF_4 and O_2 (with flowrates of 20 sccm and 2 sccm, respectively, resulting in a process pressure of $\sim 6 \times 10^{-2}$ mbar) is then used to etch through the entire 60 nm-thick stack in approximately 30 s at 25 W power. An additional 10 s oxygen plasma step, which follows the CF_4–O_2 etching, yields an increased Nb-graphene interface transparency (by typically 20%–30%). 60 nm-thick Nb contacts are then deposited using DC magnetron sputtering at a rate of $\sim$1 nm s^{-1}, with no adhesion layer deposited prior to Nb. The thickness of the Nb is chosen to match the hBN-graphene-hBN stack thickness. Lift-off is performed in acetone at a temperature of $T = 50°C$ for 20 min. A second EBL step defines the device mesa: the same RIE process used for the contacts is employed to etch the area around the devices and to define their geometry. Sample fabrication is completed with an overnight

cleaning in acetone at room temperature, to remove polymer residues.

Acknowledgments

We acknowledge financial support from the PNRR MUR Project PE0000023-NQSTI funded by the European Union-NextGenerationEU. E S acknowledges the Italian Project HELICS DFM.AD002.206. F G acknowledges the EU's Horizon 2020 Research and Innovation Framework Programme under Grants No. 964398 (SUPERGATE) and 101057977 (SPECTRUM) for partial financial support. K W and T T acknowledge support from the CREST (JPMJCR24A5), JST and World Premier International Research Center Initiative (WPI), MEXT, Japan.

Data availability statement

The data that support the findings of this study are openly available at the following URL/DOI: https://doi.org/10.5281/zenodo.22128961 [82].

Supplementary material

Additional characterization of device D1: BG-modulation of the supercurrent, Multiple Andreev Reflections, calculation of interface transparency, charge fluctuations (figure S1), extended Fraunhofer patterns of device D1 at different BG voltages (figure S2), JDE on the retrapping current, additional metric ΔI_{sw} for the JDE (figure S3), rectification efficiency as a function of different threshold values on I_{sw} (table S1), diode effect at the CNP (figure S4); data on device D2: device characterization (figure S5), diode effect (figure S6); supercurrent rectification on additional device D3 (figure S7); additional theory: details on scattering matrix formulation, diode polarity flip as a result of a mirror symmetry operation on the scattering potential (figure S8).

ORCID iDs

Ivan Villani 0009-0003-2125-5838
Luca Chirolli 0000-0002-8439-9949
Matteo Carrega 0000-0002-1956-7715
Alessandro Crippa 0000-0002-2968-611X
Elia Strambini 0000-0003-1135-2004
Francesco Giazotto 0000-0002-1571-137X
Vaidotas Mišeikis 0000-0001-6263-4250
Camilla Coletti 0000-0002-8134-7633
Fabio Beltram 0000-0002-6081-436X
Kenji Watanabe 0000-0003-3701-8119
Takashi Taniguchi 0000-0002-1467-3105
Stefan Heun 0000-0003-1989-5679
Sergio Pezzini 0000-0003-4289-907X

References

[1] Pierret R F 2003 *Advanced Semiconductor Fundamentals* (*Modular series on solid state devices*) (Prentice Hall)
[2] Ma J, Zhan R and Lin X 2025 Superconducting diode effects: mechanisms, materials and applications *Adv. Phys. Res.* **4** 2400180
[3] Davydova M, Prembabu S and Fu L 2022 Universal Josephson diode effect *Sci. Adv.* **8** eabo0309
[4] Shaffer D and Levchenko A 2025 Theories of superconducting diode effects (arXiv:2510.25864)
[5] Ando F, Miyasaka Y, Li T, Ishizuka J, Arakawa T, Shiota Y, Moriyama T, Yanase Y and Ono T 2020 Observation of superconducting diode effect *Nature* **584** 373–6
[6] Strambini E *et al* 2020 A Josephson phase battery *Nat. Nanotechnol.* **15** 656–60
[7] Zhang Y, Gu Y, Li P, Hu J and Jiang K 2022 General theory of Josephson diodes *Phys. Rev. X* **12** 041013
[8] Yuan N F Q and Fu L 2022 Supercurrent diode effect and finite-momentum superconductors *Proc. Natl Acad. Sci.* **119** e2119548119
[9] Seoane Souto R, Leijnse M and Schrade C 2022 Josephson diode effect in supercurrent interferometers *Phys. Rev. Lett.* **129** 267702
[10] He J J, Tanaka Y and Nagaosa N 2022 A phenomenological theory of superconductor diodes *New J. Phys.* **24** 053014
[11] Fukaya Y, Mercaldo M T, Margineda D, Crippa A, Strambini E, Giazotto F, Ortix C and Cuoco M 2025 Supercurrent diode with high winding vortex *Commun. Phys.* **8** 518
[12] Nagaosa N and Yanase Y 2024 Nonreciprocal transport and optical phenomena in quantum materials *Annu. Rev. Condens. Matter Phys.* **15** 63–83
[13] Misaki K and Nagaosa N 2021 Theory of the nonreciprocal Josephson effect *Phys. Rev. B* **103** 245302
[14] Tanaka Y, Lu B and Nagaosa N 2022 Theory of giant diode effect in *d*-wave superconductor junctions on the surface of a topological insulator *Phys. Rev. B* **106** 214524
[15] Fracassi S, Traverso S, Traverso Ziani N, Carrega M, Heun S and Sassetti M 2024 Anomalous supercurrent and diode effect in locally perturbed topological Josephson junctions *Appl. Phys. Lett.* **124** 242601
[16] Cayao J, Nagaosa N and Tanaka Y 2024 Enhancing the Josephson diode effect with Majorana bound states *Phys. Rev. B* **109** L081405
[17] Fracassi S, Traverso S, Heun S, Sassetti M, Carrega M and Traverso Ziani N 2025 Intrinsic and tunable superconducting diode effect in quantum spin Hall systems *Phys. Rev. B* **114** 034513
[18] Bonasera F, Falci G A, Paladino E and Pellegrino F M D 2026 From valley filtering to superconducting diode effect in spin–orbit coupled graphene junctions (arXiv:2607.06303)
[19] Baumgartner C *et al* 2022 Supercurrent rectification and magnetochiral effects in symmetric Josephson junctions *Nat. Nanotechnol.* **17** 39–44
[20] Sundaresh A, Väyrynen J I, Lyanda-Geller Y and Rokhinson L P 2023 Diamagnetic mechanism of critical current nonreciprocity in multilayered superconductors *Nat. Commun.* **14** 1628
[21] Bauriedl L *et al* 2022 Supercurrent diode effect and magnetochiral anisotropy in few-layer $NbSe_2$ *Nat. Commun.* **13** 4266
[22] Turini B, Salimian S, Carrega M, Iorio A, Strambini E, Giazotto F, Zannier V, Sorba L and Heun S 2022 Josephson diode effect in high-mobility InSb nanoflags *Nano Lett.* **22** 8502–8
[23] Pal B *et al* 2022 Josephson diode effect from Cooper pair momentum in a topological semimetal *Nat. Phys.* **18** 1228–33

[24] Lotfizadeh N, Schiela W F, Pekerten B, Yu P, Elfeky B H, Strickland W M, Matos-Abiague A and Shabani J 2024 Superconducting diode effect sign change in epitaxial Al-InAs Josephson junctions *Commun. Phys.* **7** 120

[25] Costa A *et al* 2023 Sign reversal of the Josephson inductance magnetochiral anisotropy and 0–π-like transitions in supercurrent diodes *Nat. Nanotechnol.* **18** 1266–72

[26] Baumgartner C *et al* 2022 Effect of Rashba and Dresselhaus spin–orbit coupling on supercurrent rectification and magnetochiral anisotropy of ballistic Josephson junctions *J. Phys.: Condens. Matter* **34** 154005

[27] Suri D, Kamra A, Meier T N G, Kronseder M, Belzig W, Back C H and Strunk C 2022 Non-reciprocity of vortex-limited critical current in conventional superconducting micro-bridges *Appl. Phys. Lett.* **121** 102601

[28] Hou Y *et al* 2023 Ubiquitous superconducting diode effect in superconductor thin films *Phys. Rev. Lett.* **131** 027001

[29] Greco A, Pichard Q and Giazotto F 2023 Josephson diode effect in monolithic dc-SQUIDs based on 3D Dayem nanobridges *Appl. Phys. Lett.* **123** 092601

[30] Díez-Mérida J *et al* 2023 Symmetry-broken Josephson junctions and superconducting diodes in magic-angle twisted bilayer graphene *Nat. Commun.* **14** 2396

[31] Margineda D, Crippa A, Strambini E, Fukaya Y, Mercaldo M T, Cuoco M and Giazotto F 2023 Sign reversal diode effect in superconducting Dayem nanobridges *Commun. Phys.* **6** 343

[32] Li Y *et al* 2024 Interfering Josephson diode effect in $Ta_2Pd_3Te_5$ asymmetric edge interferometer *Nat. Commun.* **15** 9031

[33] Chen S *et al* 2024 Current induced hidden states in Josephson junctions *Nat. Commun.* **15** 8059

[34] Chen P *et al* 2024 Edelstein effect induced superconducting diode effect in inversion symmetry breaking $MoTe_2$ Josephson junctions *Adv. Funct. Mater.* **34** 2311229

[35] Rashidi A, Ahadi S and Stemmer S 2025 Self-field-induced Josephson diode effect *Nano Lett.* **25** 10544–8

[36] Wu H, Wang Y, Xu Y, Sivakumar P K, Pasco C, Filippozzi U, Parkin S S P, Zeng Y-J, McQueen T and Ali M N 2022 The field-free Josephson diode in a van der Waals heterostructure *Nature* **604** 653–6

[37] Narita H *et al* 2022 Field-free superconducting diode effect in noncentrosymmetric superconductor/ferromagnet multilayers *Nat. Nanotechnol.* **17** 823–8

[38] Jeon K-R, Kim J-K, Yoon J, Jeon J-C, Han H, Cottet A, Kontos T and Parkin S S P 2022 Zero-field polarity-reversible Josephson supercurrent diodes enabled by a proximity-magnetized Pt barrier *Nat. Mater.* **21** 1008–13

[39] Strambini E *et al* 2022 Superconducting spintronic tunnel diode *Nat. Commun.* **13** 2431

[40] Lin J-X, Siriviboon P, Scammell H D, Liu S, Rhodes D, Watanabe K, Taniguchi T, Hone J, Scheurer M S and Li J I A 2022 Zero-field superconducting diode effect in small-twist-angle trilayer graphene *Nat. Phys.* **18** 1221–7

[41] Chiles J, Arnault E G, Chen C-C, Larson T F Q, Zhao L, Watanabe K, Taniguchi T, Amet F and Finkelstein G 2023 Nonreciprocal supercurrents in a field-free graphene Josephson triode *Nano Lett.* **23** 5257–63

[42] Qi S, Ge J, Ji C, Ai Y, Ma G, Wang Z, Cui Z, Liu Y, Wang Z and Wang J 2025 High-temperature field-free superconducting diode effect in high-T_c cuprates *Nat. Commun.* **16** 531

[43] Margineda D *et al* 2025 Back-action supercurrent rectifiers *Commun. Phys.* **8** 16

[44] Borgongino L, Seoane Souto R, Paghi A, Senesi G, Skibinska K, Sorba L, Riccardi E, Giazotto F and Strambini E 2025 Biharmonic-drive tunable Josephson diode *Nano Lett.* **25** 14451–8

[45] Zhang X *et al* 2024 Superconducting diode effect in a constricted nanowire *Adv. Quantum Technol.* **7** 2300378

[46] Ghosh S *et al* 2024 High-temperature Josephson diode *Nat. Mater.* **23** 612–8

[47] Satchell N, Shepley P M, Rosamond M C and Burnell G 2023 Supercurrent diode effect in thin film Nb tracks *J. Appl. Phys.* **133** 203901

[48] Coraiola M *et al* 2024 Flux-tunable Josephson diode effect in a hybrid four-terminal Josephson junction *ACS Nano* **18** 9221–31

[49] Gupta M, Graziano G V, Pendharkar M, Dong J T, Dempsey C P, Palmstrøm C and Pribiag V S 2023 Gate-tunable superconducting diode effect in a three-terminal Josephson device *Nat. Communi.* **14** 3078

[50] Matsuo S, Imoto T, Yokoyama T, Sato Y, Lindemann T, Gronin S, Gardner G C, Manfra M J and Tarucha S 2023 Josephson diode effect derived from short-range coherent coupling *Nat. Phys.* **19** 1636–41

[51] Valentini M *et al* 2024 Parity-conserving Cooper-pair transport and ideal superconducting diode in planar Germanium *Nat. Commun.* **15** 169

[52] Ciaccia C, Haller R, Drachmann A C C, Lindemann T, Manfra M J, Schrade C and Schönenberger C 2023 Gate-tunable Josephson diode in proximitized InAs supercurrent interferometers *Phys. Rev. Res.* **5** 033131

[53] Rothstein A *et al* 2026 Gate-Tunable Josephson Diodes in Magic-Angle Twisted Bilayer Graphene *Nano Lett.* **26** 2119–28

[54] Chieppa A *et al* 2025 Unveiling the current-phase relationship of InSb Nanoflag Josephson junctions using a NanoSQUID magnetometer *Nano Lett.* **25** 14412–9

[55] Ilić S, Virtanen P, Crawford D, Heikkilä T T and Sebastián Bergeret F 2024 Superconducting diode effect in diffusive superconductors and Josephson junctions with Rashba spin–orbit coupling *Phys. Rev. B* **110** L140501

[56] Bhardwaj V *et al* 2025 Gate-Tunable Orbital Magnetism and Competing Superconductivity in Twisted Trilayer Graphene Josephson Junctions *ACS Appl. Mater. Interfaces* **17** 69784–94

[57] Hu J-X, Sun Z-T, Xie Y-M and Law K T 2023 Josephson diode effect induced by valley polarization in twisted bilayer graphene *Phys. Rev. Lett.* **130** 266003

[58] Lau C N, Bockrath M W, Mak K F and Zhang F 2022 Reproducibility in the fabrication and physics of moiré materials *Nature* **602** 7895

[59] Calado V E, Goswami S, Nanda G, Diez M, Akhmerov A R, Watanabe K, Taniguchi T, Klapwijk T M and Vandersypen L M K 2015 Ballistic Josephson junctions in edge-contacted graphene *Nat. Nanotechnol.* **10** 761–4

[60] Castro Neto A H, Guinea F, Peres N M R, Novoselov K S and Geim A K 2009 The electronic properties of graphene *Rev. Mod. Phys.* **81** 109–62

[61] Rhodes D, Chae S H, Ribeiro-Palau R and Hone J 2019 Disorder in van der Waals heterostructures of 2D materials *Nat. Mater.* **18** 541–9

[62] Decker R, Wang Y, Brar V W, Regan W, Tsai H-Z, Wu Q, Gannett W, Zettl A and Crommie M F 2011 Local electronic properties of graphene on a BN substrate via scanning tunneling microscopy *Nano Lett.* **11** 2291–5

[63] Chirolli L, Greco A, Crippa A, Strambini E, Cuoco M, Amico L and Giazotto F 2025 Diode effect in the Fraunhofer pattern of disordered planar Josephson junctions *Commun. Phys.* **8** 483

[64] Villani I *et al* 2025 Quasi-Φ_0-Periodic Supercurrent at Quantum Hall Transitions *ACS Nano* **19** 27370–8

[65] Miseikis V *et al* 2015 Rapid CVD growth of millimetre-sized single crystal graphene using a cold-wall reactor *2D Mater.* **2** 014006

[66] Miseikis V, Bianco F, David J, Gemmi M, Pellegrini V, Romagnoli M and Coletti C 2017 Deterministic patterned growth of high-mobility large-crystal graphene: a path towards wafer scale integration *2D Mater.* **4** 021004

[67] Pezzini S, Mišeikis V, Pace S, Rossella F, Watanabe K, Taniguchi T and Coletti C 2020 High-quality electrical transport using scalable CVD graphene *2D Mater.* **7** 041003

[68] Ben Shalom M *et al* 2016 Quantum oscillations of the critical current and high-field superconducting proximity in ballistic graphene *Nat. Phys.* **12** 318–22
[69] Borzenets I V *et al* 2016 Ballistic graphene Josephson junctions from the short to the long junction regimes *Phys. Rev. Lett.* **117** 237002
[70] Samaddar S, Yudhistira I, Adam S, Courtois H and Winkelmann C B 2016 Charge puddles in graphene near the Dirac point *Phys. Rev. Lett.* **116** 126804
[71] Das Sarma S, Adam S, Hwang E H and Rossi E 2011 Electronic transport in two-dimensional graphene *Rev. Mod. Phys.* **83** 407–70
[72] Yao Y, Ye F, Qi X-L, Zhang S-C and Fang Z 2007 Spin–orbit gap of graphene: first-principles calculations *Phys. Rev. B* **75** 041401
[73] Island J O *et al* 2019 Spin–orbit-driven band inversion in bilayer graphene by the van der Waals proximity effect *Nature* **571** 7763
[74] Rout P, Papadopoulos N, Peñaranda F, Watanabe K, Taniguchi T, Prada E, San-Jose P and Goswami S 2024 Supercurrent mediated by helical edge modes in bilayer graphene *Nat. Commun.* **15** 856
[75] Guiducci S, Carrega M, Taddei F, Biasiol G, Courtois H, Beltram F and Heun S 2019 Full electrostatic control of quantum interference in an extended trenched Josephson junction *Phys. Rev. B* **99** 235419
[76] Turini B, Salimian S, Carrega M, Paolucci F, Zannier V, Sorba L and Heun S 2025 Side-gate modulation of supercurrent in InSb Nanoflag-based Josephson junctions *Phys. Status Solidi b* **262** 2400534
[77] Seredinski A, Draelos A W, Arnault E G, Wei M-T, Li H, Fleming T, Watanabe K, Taniguchi T, Amet F and Finkelstein G 2019 Quantum Hall-based superconducting interference device *Sci. Adv.* **5** eaaw8693
[78] Wang L *et al* 2013 One-dimensional electrical contact to a two-dimensional material *Science* **342** 614–7
[79] Purdie D G, Pugno N M, Taniguchi T, Watanabe K, Ferrari A C and Lombardo A 2018 Cleaning interfaces in layered materials heterostructures *Nat. Commun.* **9** 5387
[80] Couto N J G, Costanzo D, Engels S, Ki D-K, Watanabe K, Taniguchi T, Stampfer C, Guinea F and Morpurgo A F 2014 Random strain fluctuations as dominant disorder source for high-quality on-substrate graphene devices *Phys. Rev. X* **4** 041019
[81] Neumann C *et al* 2015 Raman spectroscopy as probe of nanometre-scale strain variations in graphene *Nat. Commun.* **6** 8429
[82] Villani I*et al* 2026 Dataset for the research work "Graphene Josephson diodes from asymmetric disorder" *Zenodo* (https://doi.org/10.5281/zenodo.22128961)